

# PROBABILISTIC FRAGILITY ANALYSIS OF COHESIVE CRACK MODELS

Mohammad Amin Hariri-Ardebili\* and Victor E. Saouma†

\*University of Colorado

Boulder, CO USA

e-mail: mohammad.haririardabili@colorado.edu

†University of Colorado

Boulder, CO USA

e-mail: saouma@colorado.edu

**Key words:** Cohesive crack; Dam; Fracture; Fragility; Uncertainty

**Abstract.** The zero thickness, fracture mechanics inspired cohesive crack model has been widely used in its various formulations. The constitutive model being formulated in terms of about fourteen parameters, yet only few can be measured experimentally, and other must be estimated.

This paper performs a sensitivity analysis to assess the relative importance of each of the parameters resulting in the model Tornado diagram. For the most sensitive parameters, uncertainty quantification is performed through Latin Hypercube Sampling to determine capacity and fragility curves. Finally, impact of correlation among the parameters is assessed.

The study is conducted by performing pushover analysis of a simple interface element under mode I and II, and dynamic analysis of a dam with joint elements subjected to mixed-mode fracture. This investigation leads to a probabilistic-based safety assessment of structures which responses is primarily governed by cohesive cracking.

## 1 Introduction

Zero thickness interface elements were first developed in the context of rock mechanics [1]. Cohesive crack models have indeed gained much acceptance as an alternative to linear elastic fracture mechanics. As to cementitious materials, the Hillerborg's cohesive crack model [2] defined a new class of fracture mechanics-based interface elements [3–6]. They are used in the context of the so-called discrete crack model (as opposed to smeared crack model) in the finite element simulation of cracking.

The cohesive elements would typically be formulated in terms of well over ten parameters (described below). A major challenge in their use is the selection of the parameters as only few can be measured experimentally, and the remaining must be estimated. Hence, a crit-

ical question is how important is the accurate estimate of each of the model parameters. This can only be achieved through sensitivity and uncertainty analyses.

Sources of uncertainty can be traced to one of eight groups [7]. Chief among them is the basic random variables (RVs),  $\mathbf{X} = (X_1, \dots, X_n)$ . The RVs in turn can be categorized as aleatory or epistemic [7]. An aleatory uncertainty is presumed to be the intrinsic randomness of a phenomenon, while an epistemic one is due to lack of knowledge. The basic qualifier refers to directly observable quantities such as material properties (strength and stiffness), loads (earthquake magnitude and sea wave height), environmental phenomena (temperature, alkali-aggregate reaction), and geometric dimensions (section size).

The study is conducted by performing pushover analysis of a simple interface element under mode I and II, and dynamic analysis of a dam with joint elements subjected to mixed-mode fracture. This investigation leads to a probabilistic-based safety assessment of structures, in the context of fragility curves, which responses is primarily governed by cohesive cracking [8].

## 2 Background; Theory

### 2.1 Interface Joint Model

As mentioned earlier, there are a number of fracture mechanics-based interface joint models; however, for the context of this paper [5] is used. It should be noted that most of the existing models are essentially mere variation of the one used. The element constitutive model is defined with respect to a general fracture and the corresponding failure surface, figure 1(a). The generalized failure surface is given by [9]

$$F = (\tau_1^2 + \tau_2^2) - 2c \tan(\phi_f)(f_t - \sigma) - \tan^2(\phi_f)(\sigma^2 - f_t^2) = 0 \quad (1)$$

where  $c$  is the cohesion,  $\phi_f$  is the angle of friction,  $f_t$  is the tensile strength of the interface,  $\tau_1$  and  $\tau_2$  are the two tangential components of the interface traction vector, and finally  $\sigma$  is the normal traction component. The shape of the 2D failure function is shown in figure 1(a). The general 3D failure function is obtained by mere rotation around the  $\sigma$ -axis.

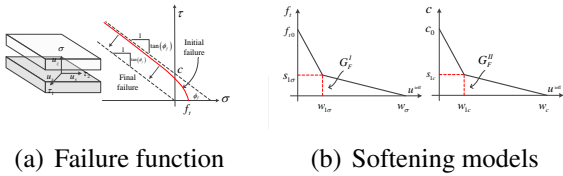


Figure 1: Zero-thickness interface joint element and corresponding failure surface

The evolution of the failure function is based on a softening parameter  $u^{ieff}$  which is the norm of the inelastic displacement vector  $u^i$ . In the present study, a bi-linear relationship is used for  $c(u^{ieff})$  and  $f_t(u^{ieff})$ , figure 1(b), where  $G_F^I$

and  $G_F^{II}$  are mode I and II fracture energies.  $s_{1c}$ ,  $w_{1c}$ ,  $s_{1\sigma}$  and  $w_{1\sigma}$  are the coordinates of the break-point in the bi-linear softening laws for cohesion and tensile strength, respectively. The critical opening and sliding corresponding to zero cohesion and tensile strength are denoted by  $w_\sigma$  and  $w_c$  respectively, and they are determined from the condition that the area under the bi-linear softening law must be equal to  $G_F^I$  and  $G_F^{II}$  respectively.

### 2.2 Sensitivity Analysis

Sensitivity analysis determines the impact of a variation in an input parameter on output results. Mathematically, this corresponds to the partial derivative of the output function (the finite element model in this case) with respect to an input parameter at a given design point.

The procedure starts with the identification of the basic RVs,  $\mathbf{X} = (X_1, \dots, X_n)$ , and their corresponding distributional model (e.g. normal, log-normal). The response can be mathematically expressed as

$$\Theta = f(X_1, X_2, \dots, X_i, \dots, X_n) \quad (2)$$

Then,  $2n + 1$  analyses are performed [10] using mean ( $X_i^{mean}$ ), minimum ( $X_i^{min}$ ) and maximum ( $X_i^{max}$ ) values of the RVs. Subsequently, the reference ( $\Theta^{Ref}$ ), the minimum ( $\Theta_i^{min}$ ) and the maximum responses ( $\Theta_i^{max}$ ) are determined. The swing for each of the  $n$  RVs is computed next

$$\Theta_i^{swing} = |\Theta_i^{max} - \Theta_i^{min}| \quad (3)$$

and are sorted in descending order. Finally, the Tornado diagram is plotted and one has to arbitrarily decide what are the most sensitive RVs, figure 2.

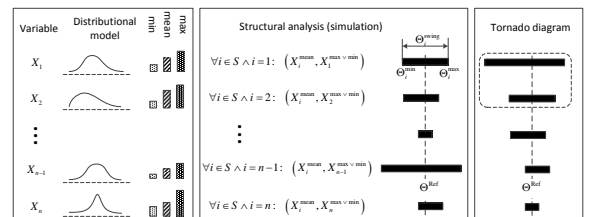


Figure 2: Sensitivity analysis using Tornado diagram

### 2.3 Uncertainty Quantification

Uncertainty arises from the probabilistic nature of the input data resulting in a non-deterministic outcome. Sampling of the distributional model is indeed a key element of an uncertainty analysis. By far, the most widely used sampling method is the so-called Monte Carlo Simulation (MCS). Success of the method hinges on a very large number of analysis as limited sampling may not include values in the outer ranges of the distribution. As a palliative to this handicap, an improved sampling method is achieved through the so-called Latin Hypercube Sampling (LHS) [11]. LHS guarantees samples to be drawn over the whole range of the distribution and proceeds as follows. Given a system with basic RVs,  $\mathbf{X} = (X_1, \dots, X_n)$  and corresponding distributions  $D_1, \dots, D_n$ , first the range of each variable is split into  $m$  non-overlapping intervals of equal marginal probability  $1/m$ . Then, sampling starts with the random selection of an interval followed by another random selection of a point inside it. The procedure is repeated until all intervals have been accessed, and none of them more than once. This procedure is repeated for each of the  $n$  RVs. Figure 3 illustrated the LHS two RVs and  $m = 8$ .

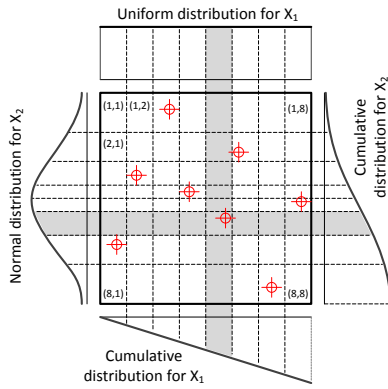


Figure 3: Illustrative example of LHS for  $\mathbf{X} = (X_1, X_2)$

So far, the RVs have been assumed to be uncorrelated. Yet at times they are, e.g. the compressive strength and elastic modulus of concrete are related by  $E = 57,000\sqrt{f'_c}$ . Thus, in

the presence of the correlated variables, the previously described algorithm for the LHS must be refined to account for the correlation matrix. This can be achieved using the Iman and Conover algorithm [11].

### 2.4 Capacity Curves

Results of structural analyses under the monotonically increased load or displacement can be expressed in term of capacity curve. The capacity curve has on its horizontal axis an engineering demand parameter (EDP) (e.g. displacement, crack length ratio, joint opening) and on the vertical one an intensity measure (IM) (e.g. peak ground acceleration (PGA) or spectral acceleration  $S_a(T)$  for dynamic analysis and applied load or displacement in a pushover analysis - POA). Capacity curve covers the full range of response from linear to non-linear and ultimately failure.

### 2.5 Fragility Curves

A fragility curve is the probability of failure (or other limit states - LS) of a system as a function of IM [12]. It is called seismic fragility curve if it is obtained from seismic analysis. A log-normal cumulative distribution function is usually used to define it

$$P[\mathcal{F} | \text{IM} = im] = \Phi \left( \frac{\ln(im) - \ln(\eta_{\mathcal{F}|\text{IM}})}{\beta_{\mathcal{F}|\text{IM}}} \right) \quad (4)$$

where  $\mathcal{F}$  corresponds to fracture,  $P[A|B]$  is the probability of occurrence of  $A$  conditioned on  $B$ ,  $\Phi(\cdot)$  is the standard normal cumulative distribution function,  $\eta_{\mathcal{F}|\text{IM}}$  median of the fragility function, and  $\beta_{\mathcal{F}|\text{IM}}$  the logarithmic standard deviation (also called dispersion). The estimated median and dispersion (logarithmic standard deviation) are given by

$$\hat{\eta}_{\mathcal{F}|\text{IM}} = \exp \left( \frac{1}{m} \sum_{i=1}^m \ln(\text{IM}_i) \right)$$

$$\hat{\beta}_{\mathcal{F}|\text{IM}} = \sqrt{\frac{1}{m-1} \sum_{i=1}^m \left( \ln \left( \frac{\text{IM}_i}{\hat{\eta}_{\mathcal{F}|\text{IM}}} \right) \right)^2} \quad (5)$$

where  $m$  is the number of simulations (number of sampling points in MCS or LHS).

### 3 Finite Element Simulations

Three representative problems are selected: (1) Mode I fracture: The response of a crack in pure mode I fracture subjected to monotonically increased displacement; (2) Mode II fracture: Similar to the preceding case, but the crack is subjected to a mode II crack sliding displacement; (3) Mixed-mode fracture: The dynamic response of a concrete dam-foundation joint is assessed using ETA method [13].

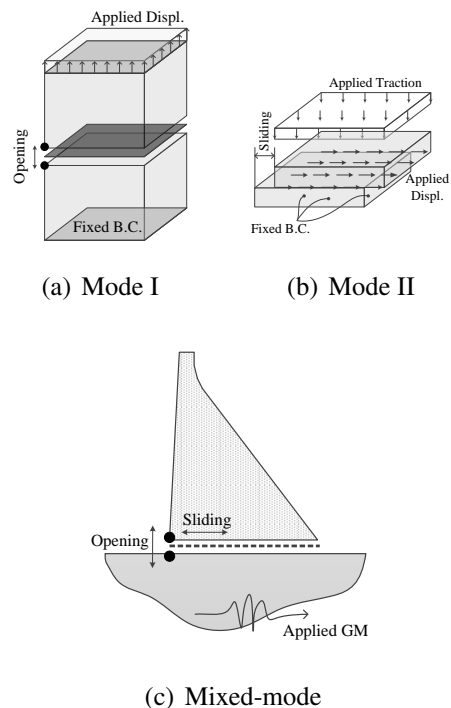


**Figure 4:** Investigated models

The finite element models of the three case studies are shown in figure 4. The mode I fracture is subjected to an imposed vertical displacement, while the mode II one is subjected to an imposed shear displacement on the lower face of the upper block (while it is also subjected to imposed compressive traction). The mixed-mode fracture is simulated through the seismic response of a rock-concrete joint.

For the present study, the fracture parameters shown in Table 1 are used. To each parameter a mean value and the coefficient of variation (COV) (which is the ratio of standard deviation to mean) is assumed based on engineering judgment. In all the cases, normal distributions are assumed and are truncated to [0.5 mean, 1.5 mean].

**Table 1:** Parameters defining the zero-thickness interface joint element

Characteristics	Symbol	Unit	Mean	COV	[Lower, Upper]
Tangential stiffness	$k_t$	GPa	224	0.2	[112, 336]
Normal stiffness	$k_n$	GPa	224	0.2	[112, 336]
Tensile strength	$f_t$	MPa	2.24	0.2	[1.12, 3.36]
Cohesion	$c$	MPa	1.90	0.2	[0.95, 2.85]
Friction angle	$\phi_f$	Deg.	38	0.2	[19, 57]
Dilatancy angle	$\phi_d$	Deg.	20	0.2	[10, 30]
Specific mode I fracture energy	$G_F^I$	N/m	252	0.2	[126, 378]
Specific mode II fracture energy	$G_F^{II}$	N/m	2520	0.2	[1260, 3780]
Relative irreversible deformation	$\gamma$	-	0.3	0.1	[0.15, 0.45]
Max. displacement for dilatancy	$u_{D_{max}}$	m	0.01	0.1	[0.005, 0.015]
Tensile stress at break-point	$s_{1\sigma}$	MPa	0.56	-	-
COD at break-point	$w_{1\sigma}$	m	1.12e-4	-	-
Cohesion at break-point	$s_{1c}$	MPa	0.475	-	-
CSD at break-point	$w_{1c}$	m	1.89E-3	-	-

## 4 Results and discussion

### 4.1 Mode I Fracture

#### 4.1.1 Sensitivity Analysis

In the presence of 14 RVs,  $2 \times 14 + 1 = 29$  displacement control POA are performed. In order to investigate the sensitivity of the results to the variation of the particular RV, two ( $r = 2$ ) sets of boundary limits are considered. First a low variation  $[0.75\eta_{RV_i}, 1.25\eta_{RV_i}]$ , and then a high variation  $[0.50\eta_{RV_i}, 1.50\eta_{RV_i}]$ . Note that  $\eta_{RV_i}$  is the median of the  $i^{th}$  RV which is equal to the mean for the normal distributions.

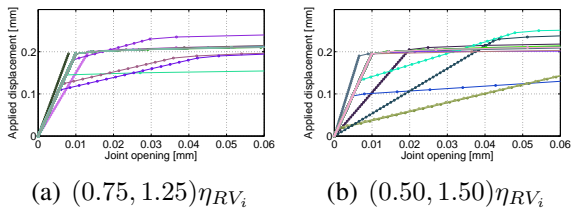


Figure 5: Capacity curves for mode I fracture

Figure 5 shows the capacity curves from the 29 POA for the two models. Response is either bi- or tri-linear. The first change in slope corresponds to fracture initiation and the second to failure. As expected the narrower band, figure 5(a), exhibits smaller dispersion than the broader one.

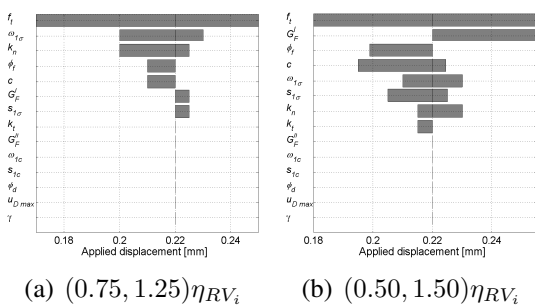


Figure 6: Tornado diagrams for the mode I fracture

The Tornado diagram corresponding to these two analyses are shown in figure 6. It is worth noting, that though this model has 14 parameters, only about half of them govern the response in mode I. By far, the dominant effect is the tensile strength  $f_t$ . This is to be anticipated given the failure envelope in figure 1(a).

In figure 6(b) the bar diagram corresponding to  $G_F^I$  indicates sensitivity to increases of the original  $G_F^I$  and not to their decrease. Likewise for some of the other eccentric values. Henceforth, in this case about half of the parameters may have to be assumed as variables, the others can be fixed.

#### 4.1.2 Uncertainty Quantification

In this case only 10 of the RVs are considered. They are all the material parameters except those defining the softening break points. Since multiple RVs are concurrently selected, one can consider either one of two cases: uncorrelated or correlated RVs. A total of  $m = 1,000$  analyses are performed for each case. Results of the correlated sampling (driven by LHS) is shown in figure 7. Correlation coefficients are selected based on engineering judgment and previous researches. The diagonal plots are the histograms of each RV (truncated normal distribution).

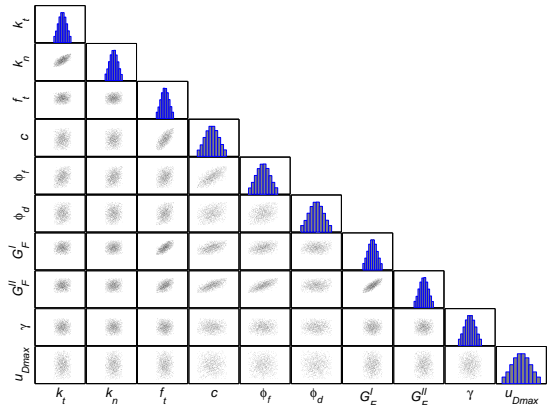
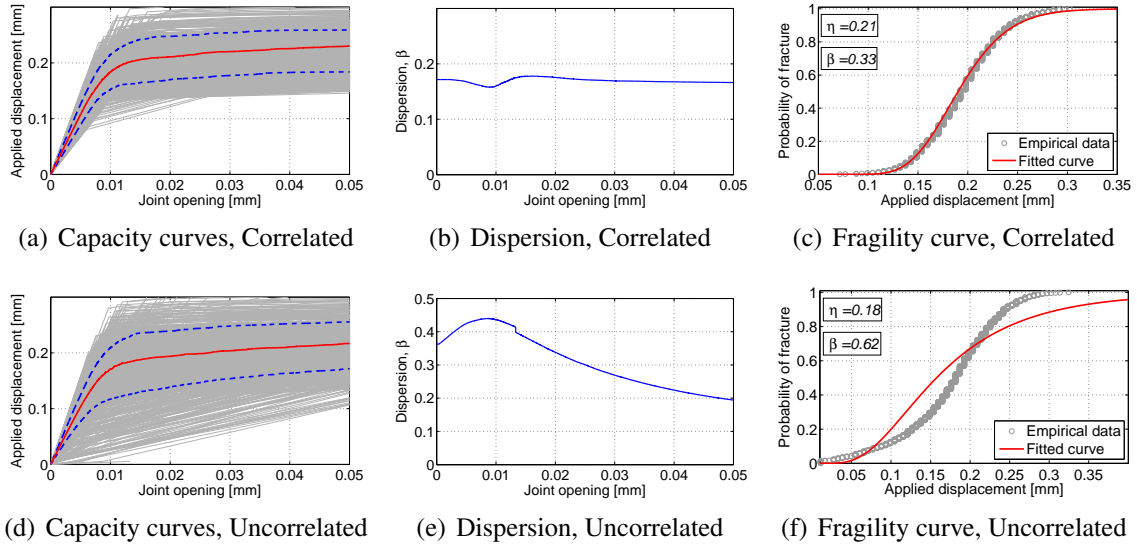


Figure 7: LHS-based correlated sampling of the RVs

Figure 8 compares the uncertainty quantification with and without correlations. The dispersion for correlated RVs is nearly constant. In the uncorrelated RVs, it peaks, then descends. In this case the dispersion is nearly twice the one of the correlated RVs. Finally, the fragility curves of the correlated case better match the empirical data points than in the uncorrelated one.



**Figure 8:** Impact of RV correlation on the uncertainty quantification of the mode I fracture

## 4.2 Mode II Fracture

### 4.2.1 Sensitivity Analysis

In this case, two plates are in contact through the zero-thickness interface element, while a normal compressive traction is applied on the top face, and displacement imposed on the lower surface of the top plate. Again, two sets of boundary limits are considered: a low variation  $[0.75\eta_{RV_i}, 1.25\eta_{RV_i}]$ , and then a high variation  $[0.50\eta_{RV_i}, 1.50\eta_{RV_i}]$ . Figure 9 shows the capacity curves resulted from POA for the two bounded models. Contrarily to the Mode I case (figure 5), the transition from linear to sliding to failure is much smoother. In the former case, the failure is indeed more brittle, whereas in this case, the presence of friction dampens the response. As before, there is a higher variation in the broad band.

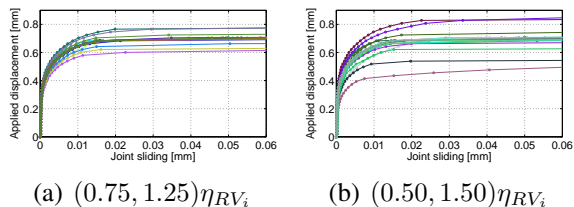


**Figure 9:** Capacity curves for the mode II fracture

Figure 10 shows the associated tornado diagram. Clearly, and as expected, cohesion  $c$  and angle of friction  $\phi_f$  are dominant. Surpris-

ingly, in this pure mode II loading,  $G_F^I$  and  $G_F^{II}$  have similar (but marginal) impact. Contrarily to Mode I, the bounds have no impact on the order of the most sensitive variables, figure 6 vs. figure 10.

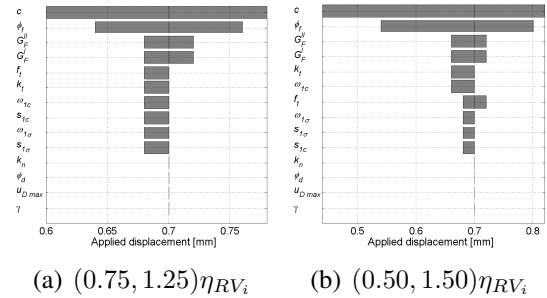


**Figure 10:** Tornado diagrams for the mode II fracture

### 4.2.2 Uncertainty Quantification

Similar to the mode I, the correlated and uncorrelated RVs are investigated for mode II, Figure 11. In both cases, the capacity functions are quite similar, while there is a discontinuity in the dispersion curve for the uncorrelated condition. The medians of the two fragility curves are identical and the dispersion of uncorrelated RVs is slightly higher than the other one. This is due to the dominant role of  $\phi_f$  and  $c$  in Mode II. Hence, and contrarily to the Mode I case, having correlated RVs does not improve the fragility curve (nearly identical dispersion).

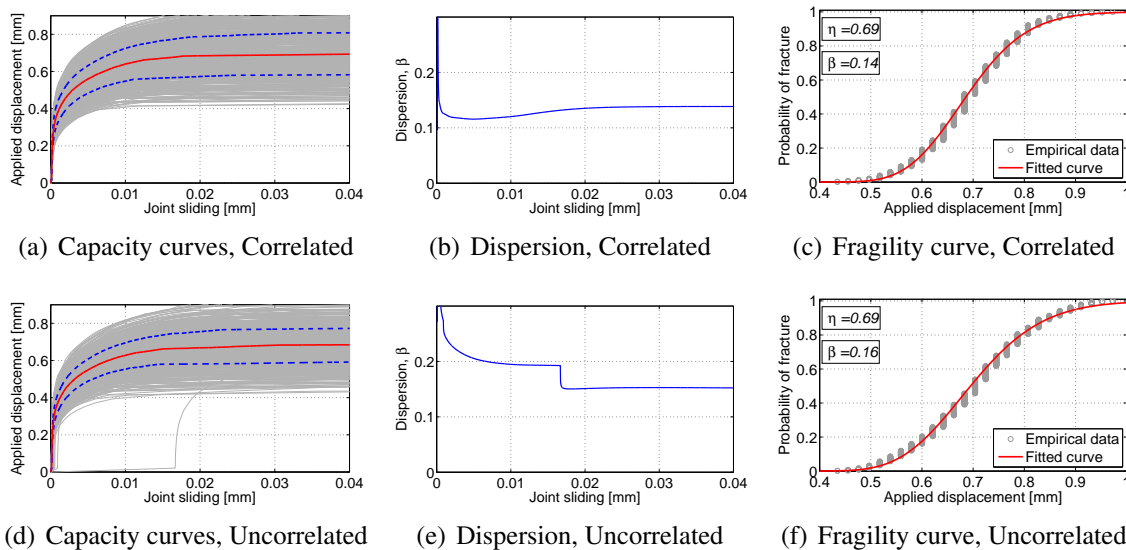


**Figure 11:** Impact of RV correlation on the uncertainty quantification of the mode II fracture

### 4.3 Mixed-Mode Fracture

Having examined two highly idealized cases, attention is now turned to a mixed mode crack propagation in a real structure: a concrete dam subjected to seismic loading, figure 4(c). In this case the nonlinear response is governed by the

one of the zero-thickness interface elements between concrete and rock. Variables associated with the joint have already been reported in Table 1 and Table 2 shows the RVs associated with concrete and rock. Four of them will be added to the list of 13 RVs:  $E_c$ ,  $\nu_c$ ,  $\rho_c$ , and  $E_f$  for a complete assessment.

**Table 2:** Characteristics of concrete and rock

Characteristics	Symbol	Unit	Mean	COV	[Lower, Upper]
Concrete modulus of elasticity	$E_c$	GPa	22.4	0.15	[15.6, 29.1]
Concrete Poisson's ratio	$\nu_c$	-	0.2	0.15	[0.14, 0.26]
Concrete tensile strength	$f_{te}$	MPa	2.24	0.20	[1.12, 3.36]
Concrete mass density	$\rho_c$	kg/m <sup>3</sup>	2500	0.10	[2000, 3000]
Foundation modulus of elasticity	$E_f$	GPa	24.0	0.15	[16.8, 31.2]
Foundation Poisson's ratio	$\nu_f$	-	0.25	0.15	[0.18, 0.32]

#### 4.3.1 Sensitivity Analysis

Sensitivity analysis will be performed for 12 RVs for the joint ( $u_{D_{max}}$  and  $\gamma$  were left out in light of their limited contribution), and the four elastic proprieties of the concrete and rock. Thus,  $2 \times 16 + 1 = 33$  observations are required.

In the spirit of this probabilistic-based fracture mechanics investigation, three separate acceleration functions are considered within the framework of the so-called ETA method [13]. This method uses 3 dynamic analyses for each case and then takes the mean response. Hence

the original 33 models have to be analyzed three times each resulting in 99 nonlinear transient analyses. In this third case, the boundary limits were arbitrarily set to  $[0.66\eta_{RV_i}, 1.33\eta_{RV_i}]$ .

Based on the mean response of the three analyses, the Tornado diagram is determined in figure 12. A major difference with the preceding two Tornado diagrams (figure 6 and 10) nearly all parameters are equally important. This implies that there are no redundant parameters in the examined model.

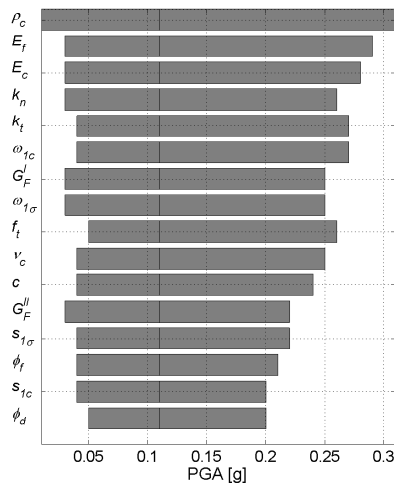


Figure 12: Tornado diagram for the mixed-mode fracture

### 4.3.2 Uncertainty Quantification

Since the preceding sensitivity analysis has determined that all RVs are nearly equally relevant, the uncertainty quantification will retain them all. For each set of uncertainty, 100 simulations are performed. Again, two set of analyses will be reported. In the first one RV is sampled at a time, in the second, all the RVs are sampled simultaneously. Furthermore, whereas in the first two cases there was only a single LS which indicated failure, in the case of a dam, four of them are identified. They correspond to crack length over the total base. Four distinct ones are selected 10%, 30%, 60%, and 99% [13].

**Single RV:** It was determined that nearly all the fragility curves corresponding to a given  $LS_i$  ( $i = 1, 2, 3, 4$ ) are identical. This confirms the results of sensitivity analysis in figure 12. To better quantify the results, the median and dispersion are separately shown in figure 13. It is noted that the median at  $LS=0.10$  and  $LS=0.30$  are almost identical for all RVs. The median at  $LS=0.60$  and  $LS=0.99$  vary for different RVs yet have the same trend. Another notable observation is that the dispersion of  $RV1 = \rho_c$  is about twice the next highest one. This can be ex-

plained by the fact that in the context of the seismic analysis, proper evaluation of the mass is essential.

**Multiple RV:** Correlated and uncorrelated RVs when they are all modified simultaneously are shown in figure 14. It is clear that in this process the range of capacity curves go from nearly zero to a maximum. The former is induced by a random selection of unfavorable RVs across the board. Examination of the damage index reveals that higher PGAs are needed to trigger larger limit states. Results for correlated an uncorrelated values are nearly identical. The fragility curves confirm the brittle nature of the problem, where difference between  $LS=0.10$  and  $0.30$  is small; however the one between  $0.30$  and  $0.60$  is substantially larger. Accounting for correlation reduces the dispersion of fragility curves, Table 3.

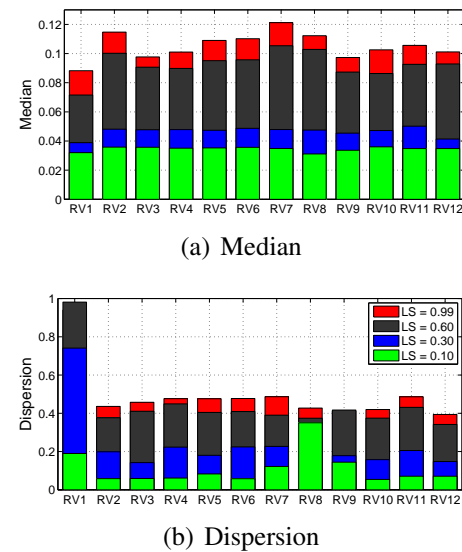
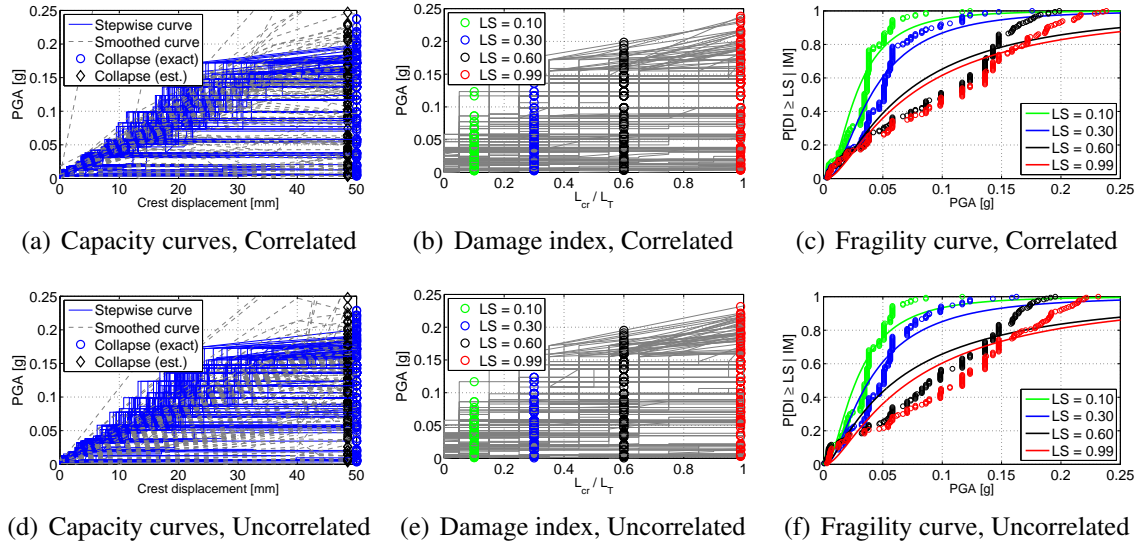


Figure 13: Comparison of all RVs for four LSs under mixed-mode fracture condition

**Table 3:** Dispersions  $\beta$  of dam analyses

LS	0.10	0.30	0.60	0.99
Correlated	0.78	0.82	1.03	1.06
Un-correlated	0.85	0.91	1.21	1.12



**Figure 14:** Impact of RV correlation on the uncertainty quantification of the mixed-mode fracture

## 5 Summary and Conclusions

The main source of nonlinearity in numerous failure simulations is indeed the fracture (Mode I and/or II) of the solid, whereas the body remains linear. A major handicap of this approach is the proper selection of the numerous material properties required by their constitutive models. Whereas few can indeed be measured experimentally, others have to be deduced, or obtained through system identification. The uncertainty caused by this arbitrary selection calls for a more rigorous quantification of the potential error.

This paper was an attempt to elucidate the importance of the fourteen parameters defining a fracture mechanics based zero thickness cohesive crack model. This is achieved within the framework of a rigorous probabilistic approach.

Most of the results confirm what may be intuitively guessed, the procedure quantifies for the first time their importance. Among the other unanticipated conclusions, one can mention:

1. The bi- and tri-linear form of the capacity curve in mode I fracture *vs.* the smoothed curve for Mode II fracture.
2. Importance of the boundary variation,  $(1 - e, 1 + e)\eta_{RV_i}$ , for Mode I fracture, while it does not affect the tornado dia-

gram in Mode II fracture.

3. Four completely different form of capacity curves in Mode I, while all curves in Mode II are nearly identical.
4. There is a discontinuity in dispersion curves of the Mode I, while they are uniform in Mode II.
5. Better correlation of fitted fragility curve and the empirical data points in Mode II single RVs than Mode I.
6. Priority in using correlated RVs than to un-correlated one for Mode I and mixed-mode fracture, while its effect is negligible in Mode II.
7. Determining 5 most sensitive RVs in Mode I and 3 in Mode II; however, in mixed mode all of the RVs are nearly important.

Those findings should provide guidance for analysts seeking to use similar zero thickness cohesive crack models in their studies.

## REFERENCES

- [1] Goodman, R.E. and Taylor, R.C. and Brekke, T.C. A Model for the Mechanics of Jointed Rocks. *J. of the Soil Me-*

- chanics and Foundations Division ASCE*, 94:637–659, 1968.
- [2] A. Hillerborg, M. Modéer, and P.E. Petersson. Analysis of crack formation and crack growth in concrete by means of fracture mechanics and finite elements. *Cement and Concrete Research*, 6(6):773–782, 1976.
- [3] H.R. Lotfi and P.B. Shing. Interface model applied to fracture masonry structures. *ASCE J. of Engineering Mechanics*, 120(1):63–79, 1994.
- [4] I. Carol, P.C. Prat, and C.M. Lopez. Normal/shear cracking model: Application to discrete crack analysis. *ASCE Journal of Engineering Mechanics*, 123(8), August 1997.
- [5] J. Cervenka, J.M. Chandra, and V. Saouma. Mixed mode fracture of cementitious bimaterial interfaces; Part II: Numerical simulation. *Engineering Fracture Mechanics*, 60(1):95–107, May 1998.
- [6] Giuseppe Cocchetti, Giulio Maier, and X.P. Shen. Piecewise linear models for interfaces and mixed mode cohesive cracks. *CMES*, 3:279–298, 2002.
- [7] A. Der-Kiureghian and O. Ditlevsen. Aleatory or epistemic? does it matter? *Structural Safety*, 31:105–112, 2009.
- [8] M.A. Hariri-Ardebili and V.E. Saouma. Sensitivity and uncertainty quantification of the cohesive crack model. *Engineering Fracture Mechanics*, 155:18–35, 2016.
- [9] Ignacio Carol, Zdeněk P. Bažant, and Pere C. Prat. Microplane type constitutive models for distributed damage and localized cracking in concrete structures. In Zdeněk P. Bažant, editor, *Proc. Fracture Mechanics of Concrete Structures*, pages 299–304. Elsevier, June 1992.
- [10] Army Corps of Engineers. Reliability assessment of navigation structures. ETL 1110-2-532, Department of the Army, US Army Corps of Engineers, Washington, D.C., May 1992.
- [11] R. Iman and W.J. Conover. A distribution-free approach to inducing rank correlation among input variables. *Communications in Statistics-Simulation and Computation*, B11:311–334, 1982.
- [12] J.W. Baker. Efficient analytical fragility function fitting using dynamic structural analysis. *Earthquake Spectra*, 31(1):579–599, 2015.
- [13] M.A. Hariri-Ardebili and V.E. Saouma. Quantitative failure metric for gravity dams. *Earthquake Engineering and Structural Dynamics*, 44:461–480, 2015.